

# The frequency detuning correction and the asymmetry of line shapes: The far wings of $\text{H}_2\text{O}-\text{H}_2\text{O}$

Q. Ma<sup>a)</sup>

*Department of Applied Physics, Columbia University, and Institute for Space Studies,  
Goddard Space Flight Center, New York, New York 10025*

R. H. Tipping

*Department of Physics & Astronomy, University of Alabama, Tuscaloosa, Alabama 35487-0324*

(Received 19 September 2001; accepted 27 November 2001)

A far-wing line shape theory that satisfies the detailed balance principle is applied to the  $\text{H}_2\text{O}-\text{H}_2\text{O}$  system. Within this formalism, two line shapes are introduced, corresponding to band averages over the positive and negative resonance lines, respectively. Using the coordinate representation, the two line shapes can be obtained by evaluating 11-dimensional integrations whose integrands are a product of two factors. One depends on the interaction between the two molecules and is easy to evaluate. The other contains the density matrix of the system and is expressed as a product of two three-dimensional distributions associated with the density matrices of the absorber and the perturber molecule, respectively. If most of the populated states are included in the averaging process, to obtain these distributions requires extensive computer CPU time, but only have to be computed once for a given temperature. The 11-dimensional integrations are evaluated using the Monte Carlo method, and in order to reduce the variance, the integration variables are chosen such that the sensitivity of the integrands on them is clearly distinguished. Numerical tests show that by taking into account about  $10^7$  random selections, one is able to obtain converged results. We find that it is necessary to consider frequency detuning, because this makes significant and opposite contributions in the two band-averaging processes and causes the lines to be asymmetric. Otherwise, the two line shapes become symmetric, are the same, and equal to the mean of the two shapes obtained including the frequency detuning effects. For the pure rotational band, we find that the magnitude of the line shape obtained from the positive line average is larger than that obtained from the negative line average for  $\omega > 0$  and vice versa for  $\omega < 0$ , and their relative gap increases as the frequency displacement from the line center increases. By adopting a realistic potential model and optimizing its parameters, one is able to obtain these two line shapes and calculate the corresponding absorption coefficients that are in good agreement with laboratory data. Also, this same potential yields good theoretical values for other physical properties of the dilute  $\text{H}_2\text{O}$  gas.

© 2002 American Institute of Physics. [DOI: 10.1063/1.1436115]

## I. INTRODUCTION

In previous papers, we have presented the theory for the calculation of far-wing line shapes and the corresponding absorption coefficients for interacting pairs of molecules.<sup>1-3</sup> Assuming only the binary collision and quasistatic approximations, we have shown that by using the coordinate representation to describe the orientation of each molecule before and after the transition, we are able to reduce the problem to the calculation of multidimensional integrals. The dimensionality of the integrals depends on the type of molecules involved; specifically for two linear molecules (e.g.,  $\text{CO}_2-\text{CO}_2$  or  $\text{CO}_2-\text{N}_2$ ) the dimensionality is 7, while for one asymmetric top and a linear partner (e.g.,  $\text{H}_2\text{O}-\text{N}_2$ ) it is 9. For the first case we were able to obtain converged results with a sophisticated interaction potential using conventional integration methods.<sup>1</sup> However, for the latter case, we had to

use the Monte Carlo method.<sup>3</sup> This system is important in atmospheric applications where we have shown that the absorption (known as the “foreign continuum”) is in good agreement with experimental results.<sup>3</sup> Because the absorption by  $\text{H}_2\text{O}-\text{H}_2\text{O}$  pairs (the “self-continuum”) is more important, we would like to extend our theory to the case of two interacting asymmetric tops; the dimensionality in this case is 11, thus implying a big challenge to obtain converged results. In a previous paper, we have shown that by considering an interaction potential containing cyclic coordinates, the dimensionality is reduced to 7, and one can obtain converged results.<sup>2</sup>

One of our goal in the present paper is to remove this restriction and calculate the far-wing line shape for  $\text{H}_2\text{O}-\text{H}_2\text{O}$  using the most general interaction potential. To accomplish this goal, it is necessary to modify the Monte Carlo routine used previously such that the sensitivity of the integrand on the integration variables is clearly characterized. A second goal is to investigate the asymmetry of line

<sup>a)</sup>Electronic mail: gma@giss.nasa.gov

shapes; in order to do this, one has to carry out band averages in a more sophisticated way and consider the frequency detuning effect in the line shape calculations. Based on the present work, one can conclude that the band-average line shapes are asymmetric and, in addition, one would expect different line shapes for different bands.

In order to reduce any unphysical effects in calculated results, we carry out all numerical calculations based on formulas that satisfy the detailed balance principle exactly and have a higher accuracy in the short-time limit.<sup>4</sup> As expected, this increases the difficulty because the formulas become more complicated. Thanks to great advances in computers made in recent years, we are able to overcome this obstacle successfully. Finally, we utilize a realistic interaction potential applicable for the dilute H<sub>2</sub>O gas that not only gives good agreement between theory and experimental temperature-dependent second virial coefficients and differential scattering cross sections, but also yield absorption coefficients that are in good agreement with the experimental self-continuum data. We note that because the theory has a sound physical basis, we expect that theoretical results calculated at a lower temperature, which would be extremely difficult to obtain experimentally because of the lower vapor pressure attainable, are valid.

The paper is organized in the following way. In Sec. II A, we present the expressions for the correlation functions and the spectral densities that satisfy detailed balance exactly. In Sec. II B, we introduce two band averages and the corresponding line shape functions. The application of the coordinate representation for the system consisting of two asymmetric tops is presented in Sec. II C. Our main purpose is to introduce the density matrices of the absorber and the perturber molecule, which are three-dimensional distributions, and to show how to calculate them. This is the most costly calculation in the present study and the results obtained are used to get the line shapes later. In Sec. II D, we discuss how to calculate the frequency detuning correction. The method is similar to that used to calculate the line shapes without this correction, except one has to develop a new technique to deal with the integrand containing a derivative. The necessary generalization of the Monte Carlo method to 11-dimensional integrations is discussed in Sec. II E. In Sec. II F, we discuss a realistic interaction potential that gives good agreement with various molecular data measured in the dilute gas phase, including the absorption coefficient. Then in Sec. II G, we apply the theory to obtain two line shape functions numerically for several temperatures and discuss some of their general features. We use these results to calculate the corresponding absorption coefficients and compare those obtained in the 300–1100 cm<sup>-1</sup> spectral region for the room temperature with experimental results. In Sec. III, we discuss the results obtained and the conclusions drawn from the present study.

The present work, together with the previous calculations for simpler systems, constitute a general formalism in which one can obtain from first principles the far-wing line shapes for any colliding pair for which a realistic potential is available. Conversely, if experimental data for the line shape or the corresponding absorption coefficients are available,

one can use this formalism in order to test the accuracy of the potentials.

## II. THE GENERAL FORMALISM

### A. Symmetric correlation function and spectral density that satisfy the detailed balance principle

The absorption coefficient  $\alpha(\omega)$  of a gaseous sample with a unit volume is given by

$$\alpha(\omega) = \frac{4\pi^2}{3\hbar c} n_a \omega \tanh(\beta\hbar\omega/2) [F(\omega) + F(-\omega)], \quad (1)$$

where  $n_a$  is the number density of absorber molecules and the spectral density,  $F(\omega)$ , is the Fourier transform of the correlation function  $C(t)$ . One separates the total Hamiltonian  $H$  into two parts: one commutes with the internal coordinates of the molecules while the second does not. We note that this distinction of  $H$  usually coincides with the division of the interaction into two parts:  $V_{\text{iso}}$  and  $V_{\text{ani}}$ , the isotropic and the anisotropic interactions, respectively. Accordingly, the total Hamiltonian  $H$  is decomposed as

$$H = H_a + H_b + V_{\text{iso}} + V_{\text{ani}} \equiv H_0 + V_{\text{ani}}, \quad (2)$$

where  $H_a$  and  $H_b$  are the unperturbed Hamiltonians of the absorber and the bath molecules, respectively. In practice, for atmospheric applications where the gas pressures are low, one can introduce the binary collision approximation and focus on a much simpler system consisting of one absorber and one bath molecule. For simplicity, we do not introduce new symbols for the two-molecule system.

It has been shown that one is able to express  $C(t)$  in the  $t \rightarrow 0$  limit, which is valid to order  $t^2$ , as<sup>4</sup>

$$C(t) = n_b \nu \text{Tr} \{ (e^{iL_a t/2} \sqrt{\rho_b \rho_a} \boldsymbol{\mu})^\dagger \rho_{\text{iso}} e^{-\beta V_{\text{ani}}} \times [e^{-iL_{\text{ani}} t} (e^{-iL_a t/2} \sqrt{\rho_b \rho_a} \boldsymbol{\mu})] \}, \quad (3)$$

where  $n_b$  is the number density of the bath molecules,  $\nu = \text{Tr}[e^{-\beta H_0}]/\text{Tr}[e^{-\beta H}]$ , and the Liouville operators  $L_a$  and  $L_{\text{ani}}$  corresponding to  $H_a$  and  $V_{\text{ani}}$ , respectively, have been introduced. For later convenience, we can introduce a symmetric correlation function  $\tilde{C}(t) [\equiv C(t + i\hbar\beta/2)]$ , defined by

$$\tilde{C}(t) = n_b \nu \text{Tr} \{ (e^{iL_a t/2} \sqrt{\rho_b \rho_a}^{1/4} \boldsymbol{\mu} \rho_a^{1/4})^\dagger \rho_{\text{iso}} e^{-\beta V_{\text{ani}}/2} \times [e^{-iL_{\text{ani}} t} (e^{-iL_a t/2} \sqrt{\rho_b \rho_a}^{1/4} \boldsymbol{\mu} \rho_a^{1/4})] e^{-\beta V_{\text{ani}}/2} \}. \quad (4)$$

From these expressions, it is easy to verify that  $C(-t) = C(t + i\hbar\beta)$  and  $\tilde{C}(-t) = \tilde{C}(t)$ , which guarantees both of them satisfy the detailed balance principle.<sup>4,5</sup>

By expressing  $\tilde{C}(t)$  explicitly as summations over indices  $i, j, i'$ , and  $j'$ , where each represents all the quantum numbers necessary to specify the energy levels of the absorber molecule, one is able to write  $\tilde{C}(t)$  as

$$\begin{aligned}\tilde{C}(t) = & \sum_{ij} \sum_{i'j'} e^{i(\omega_{ji} + \omega_{j'i'})t/2} n_b \nu \text{Tr}_b \{ \langle j | \rho_a^{1/4} \boldsymbol{\mu}^\dagger \rho_a^{1/4} \sqrt{\rho_b} | i \rangle \\ & \times \langle i | \rho_{\text{iso}} e^{-\beta V_{\text{ani}}/2} e^{-iV_{\text{ani}}t} | i' \rangle \langle i' | \sqrt{\rho_b} \rho_a^{1/4} \boldsymbol{\mu} \rho_a^{1/4} | j' \rangle \\ & \times \langle j' | e^{iV_{\text{ani}}t} e^{-\beta V_{\text{ani}}/2} | j \rangle \}. \quad (5)\end{aligned}$$

In the above expression,  $\omega_{ji} = E_j - E_i$ , and the subscript  $b$  of trace denotes the trace over the remaining variables, including all magnetic quantum numbers. We assume that the interaction between two molecules does not depend on their vibrational quantum numbers. As a result, in Eq. (5) the vibrational quantum numbers of  $i$  and  $i'$  are identical and those of  $j$  and  $j'$  are also identical, but the former could differ from the latter. By choosing the  $Z$  axis of the space-fixed frame along the separation between the two molecules, the interaction  $V_{\text{ani}}(r, \boldsymbol{\Omega}_a, \boldsymbol{\Omega}_b)$  depends on the orientations of the two molecules represented by  $\boldsymbol{\Omega}_a$  and  $\boldsymbol{\Omega}_b$ , respectively, and on  $r$ , the distance between the centers of mass, which can be considered as a parameter since the translational motion is treated classically. In Hilbert space associated with the internal degrees, one denotes the eigenvalues and eigenvectors of  $V_{\text{ani}}(r, \boldsymbol{\Omega}_a, \boldsymbol{\Omega}_b)$  by  $G_\zeta$  and  $|\zeta\rangle$ , respectively; thus

$$V_{\text{ani}}(r, \boldsymbol{\Omega}_a, \boldsymbol{\Omega}_b) |\zeta\rangle = G_\zeta(r) |\zeta\rangle. \quad (6)$$

Then, by performing the Fourier transform of the correlation function  $\tilde{C}(t)$  and carrying out an integration over  $r$  (i.e., the classical ensemble average over  $r$ , which is valid within the quasistatic approximation), one is able to obtain the symmetric spectral density  $\tilde{F}(\omega)$ ,

$$\tilde{F}(\omega) = \frac{1}{\pi} \sum_{ij} \sum_{i'j'} \tilde{\chi}_{ij;i'j'} \left[ \omega - \frac{1}{2} (\omega_{ji} + \omega_{j'i'}) \right]. \quad (7)$$

The explicit expression for  $\tilde{\chi}_{ij;i'j'}(\omega)$  is given by

$$\begin{aligned}\tilde{\chi}_{ij;i'j'}(\omega) = & \sum_{\xi\eta} \tilde{H}_{\xi\eta}(\omega) \sum_{\{m\}} \sum_{i_b} \sum_{i'_b} \langle \eta | j i_b \rangle \\ & \times \langle j i_b | \rho_a^{1/4} \boldsymbol{\mu}^\dagger \rho_a^{1/4} \sqrt{\rho_b} | i i_b \rangle \langle i i_b | \zeta \rangle \langle \zeta | i' i'_b \rangle \\ & \times \langle i' i'_b | \sqrt{\rho_b} \rho_a^{1/4} \boldsymbol{\mu} \rho_a^{1/4} | j' i'_b \rangle \langle j' i'_b | \eta \rangle, \quad (8)\end{aligned}$$

where  $i_b$  and  $i'_b$  are indices used to specify the states of the bath molecule and  $\{m\}$  indicates the summation over all magnetic quantum numbers. In the above expression,  $\tilde{H}_{\xi\eta}(\omega)$  is defined by

$$\tilde{H}_{\xi\eta}(\omega) = n_b \nu 4 \pi^2 r_c^2 \left| \frac{1}{G'_{\xi\eta}(r_c)} \right| e^{-\beta V_{\text{iso}}(r_c) - \beta [G_\xi(r_c) + G_\eta(r_c)]/2}, \quad (9)$$

where  $G'_{\xi\eta}(r)$  denotes  $(d/dr)[G_\xi(r) - G_\eta(r)]$ , and  $r_c$  are roots of the equation

$$G_\xi(r_c) - G_\eta(r_c) = \omega. \quad (10)$$

We note that in Eq. (7), the summation indices  $i, j, i'$ , and  $j'$  exclude their magnetic quantum numbers since the summation over them has been carried out. The functions  $\tilde{\chi}_{ij;i'j'}(\omega)$  introduced above are symmetric for the exchange of indices  $\{ij\} \leftrightarrow \{i'j'\}$ . Meanwhile, with respect the ex-

changes  $\{ij\} \rightarrow \{ji\}$  and  $\{i'j'\} \rightarrow \{j'i'\}$ , it is easy to verify that  $\tilde{\chi}_{ji;j'i'}(-\omega) = \tilde{\chi}_{ij;i'j'}(\omega)$ .<sup>4</sup> In terms of  $\tilde{F}(\omega)$ , the absorption coefficient  $\alpha(\omega)$  becomes

$$\alpha(\omega) = \frac{8\pi^2}{3\hbar c} n_a \omega \sinh(\beta \hbar \omega/2) \tilde{F}(\omega). \quad (11)$$

Finally, it is worth mentioning that  $\tilde{F}(\omega) = e^{-\beta \hbar \omega/2} F(\omega)$  and  $\tilde{F}(-\omega) = \tilde{F}(\omega)$ . The latter is required by the detailed balance principle.

## B. The averaged line shapes with the frequency detuning correction

We consider a band consisting of transitions between states with two vibrational quantum numbers specified. For simplicity, we designate a pair of  $i$  and  $j$  (i.e., a line) by the symbol  $k$ . If necessary, we use symbols  $k_+$  and  $k_-$  to distinguish a positive resonance line with  $E_j - E_i > 0$  and a negative resonance one with  $E_j - E_i < 0$ . Then Eq. (7) can be expressed as

$$\begin{aligned}\tilde{F}(\omega) = & \frac{1}{\pi} \left( \sum_{k_+} \sum_n \tilde{\chi}_{k_+;n} \left[ \omega - \frac{1}{2} (\omega_{k_+} + \omega_n) \right] \right. \\ & \left. + \sum_{k_-} \sum_n \tilde{\chi}_{k_-;n} \left[ \omega + \frac{1}{2} (\omega_{k_+} - \omega_n) \right] \right), \quad (12)\end{aligned}$$

where  $\omega_{k_+} (\equiv |\omega_{ji}|)$  is positive. We note that in Eq. (12) we have not explicitly characterized the symbol  $n$  by  $+$  or  $-$  yet. For the pure rotational band resulting from transitions without changing the vibrational quantum number, both the symbols  $n$  in two terms of Eq. (12) could be  $n_+$  and  $n_-$  because there is no link between the choices of  $k$  and  $n$ . Meanwhile, for a vibrational band,  $k_+$  or  $k_-$  is always associated with  $n_+$  or  $n_-$ , respectively. In this case,  $i$  and  $i'$ , and also  $j$  and  $j'$ , share the common vibrational quantum numbers and, in general, these two different vibrational quantum numbers determine whether  $k$  (i.e., a pair of  $i$  and  $j$ ) and  $n$  (i.e., a pair of  $i'$  and  $j'$ ) belong to the positive or the negative resonance. Therefore, for the vibrational bands the symbol  $n$  in the first term of Eq. (12) should be understood as  $n_+$  and in the second term as  $n_-$ . This custom is applicable for the equations following.

On the other hand, by introducing two common line shape functions  $\tilde{\chi}_+(\omega)$  and  $\tilde{\chi}_-(\omega)$  one assume that  $\tilde{F}(\omega)$  can be expressed as

$$\begin{aligned}\tilde{F}(\omega) = & \frac{1}{\pi} \left[ \sum_{k_+} \rho_k |\boldsymbol{\mu}_k|^2 \left( \frac{1}{(\omega - \omega_{k_+})^2} \tilde{\chi}_+(\omega - \omega_{k_+}) \right. \right. \\ & \left. \left. + \frac{1}{(\omega + \omega_{k_+})^2} \tilde{\chi}_-(\omega + \omega_{k_+}) \right) \right], \quad (13)\end{aligned}$$

where  $\boldsymbol{\mu}_k (\equiv \boldsymbol{\mu}_{ij})$  is the reduced dipole matrix element and  $\rho_k \equiv \sqrt{\rho_i \rho_j}$ . In order to find expressions for  $\tilde{\chi}_+(\omega)$  and  $\tilde{\chi}_-(\omega)$ , one performs the Fourier transform for Eqs. (12) and (13) and compares the results to their time-domain versions. As a result, the following equation has to be satisfied:

$$\begin{aligned}
& \sum_{k_+} \sum_n \tilde{\chi}_{k_+,n}(t) e^{i(\omega_{k_+} + \omega_n)t/2} \\
& + \sum_{k_-} \sum_n \tilde{\chi}_{k_-,n}(t) e^{-i(\omega_{k_+} - \omega_n)t/2} \\
& = \mathcal{F} \left[ \frac{1}{\omega^2} \tilde{\chi}_+(\omega) \right] \sum_{k_+} \rho_k |\boldsymbol{\mu}_k|^2 e^{i\omega_{k_+}t} \\
& + \mathcal{F} \left( \frac{1}{\omega^2} \tilde{\chi}_-(\omega) \right) \sum_{k_-} \rho_k |\boldsymbol{\mu}_k|^2 e^{-i\omega_{k_+}t}, \quad (14)
\end{aligned}$$

where for simplifying the notations we use the symbols  $\tilde{\chi}_{k_+,n}(t)$ ,  $\tilde{\chi}_{k_-,n}(t)$ ,  $\mathcal{F}[(1/\omega^2)\tilde{\chi}_+(\omega)]$ , and  $\mathcal{F}[(1/\omega^2)\tilde{\chi}_-(\omega)]$  to represent the Fourier transforms of  $\tilde{\chi}_{k_+,n}(\omega)$ ,  $\tilde{\chi}_{k_-,n}(\omega)$ ,  $(1/\omega^2)\tilde{\chi}_+(\omega)$ , and  $(1/\omega^2)\tilde{\chi}_-(\omega)$ , respectively. Furthermore, one assumes that one can separate Eq. (14) into two equations: one associated with a summation over the positive resonance lines and the other over the negative resonance lines,

$$\begin{aligned}
\mathcal{F} \left( \frac{1}{\omega^2} \tilde{\chi}_+(\omega) \right) &= \sum_{k_+} \sum_n \tilde{\chi}_{k_+,n}(t) e^{i(\omega_{k_+} + \omega_n)t/2} / \\
&\sum_{s_+} \rho_s |\boldsymbol{\mu}_s|^2 e^{i\omega_{s_+}t}, \quad (15)
\end{aligned}$$

and

$$\begin{aligned}
\mathcal{F} \left( \frac{1}{\omega^2} \tilde{\chi}_-(\omega) \right) &= \sum_{k_-} \sum_n \tilde{\chi}_{k_-,n}(t) e^{-i(\omega_{k_+} - \omega_n)t/2} / \\
&\sum_{s_+} \rho_s |\boldsymbol{\mu}_s|^2 e^{-i\omega_{s_+}t}. \quad (16)
\end{aligned}$$

Then, with Eq. (15) it is easy to obtain an expression for  $\mathcal{F}[(1/\omega^2)\tilde{\chi}_+(\omega)]$  that is valid in the short-time limit:

$$\begin{aligned}
& \mathcal{F} \left( \frac{1}{\omega^2} \tilde{\chi}_+(\omega) \right) \\
& \simeq \frac{1}{N} \sum_{k_+} \sum_n \tilde{\chi}_{k_+,n}(t) e^{i[(\omega_{k_+} + \omega_n)/2 - \bar{\omega}]t}, \quad (17)
\end{aligned}$$

where  $N$  is the normalization factor defined by

$$N = \sum_{k_+} \rho_k |\boldsymbol{\mu}_k|^2, \quad (18)$$

and  $\bar{\omega}$  is the average positive resonance frequency defined by

$$\bar{\omega} = \frac{1}{N} \sum_{k_+} \rho_k |\boldsymbol{\mu}_k|^2 \omega_{k_+}. \quad (19)$$

By performing the inverse Fourier transformation, one is able to derive the expression for  $\tilde{\chi}_+(\omega)$  valid at  $|\omega| \rightarrow \infty$ ,

$$\tilde{\chi}_+(\omega) = \omega^2 \frac{1}{N} \sum_{k_+} \sum_n \tilde{\chi}_{k_+,n} \left[ \omega - \frac{1}{2}(\omega_{k_+} + \omega_n) + \bar{\omega} \right]. \quad (20)$$

Similarly, one can derive

$$\tilde{\chi}_-(\omega) = \omega^2 \frac{1}{N} \sum_{k_-} \sum_n \tilde{\chi}_{k_-,n} \left[ \omega + \frac{1}{2}(\omega_{k_+} - \omega_n) - \bar{\omega} \right]. \quad (21)$$

In Eqs. (20) and (21) the arguments of functions depend on the summation indices and this results in difficulty obtaining  $\tilde{\chi}_+(\omega)$  and  $\tilde{\chi}_-(\omega)$  directly. In practice, one prefers to derive an expressions for  $\tilde{\chi}_+(\omega)$  and  $\tilde{\chi}_-(\omega)$  in which the summations are performed over functions whose arguments are independent of the summation indices. For this purpose, the frequency detuning approximation must be introduced. As an example, we consider Eq. (20). With the Taylor series expansion of  $\tilde{\chi}_{k_+,n}[\omega - \frac{1}{2}(\omega_{k_+} + \omega_n) + \bar{\omega}]$  over  $\omega$ , one can approximate  $\tilde{\chi}_+(\omega)$  as

$$\begin{aligned}
\tilde{\chi}_+(\omega) &= \hat{\chi}_+(\omega) \\
&+ \omega^2 \frac{1}{N} \sum_{k_+} \sum_n \left[ \bar{\omega} - \frac{1}{2}(\omega_{k_+} + \omega_n) \right] \tilde{\chi}'_{k_+,n}(\omega), \quad (22)
\end{aligned}$$

where

$$\hat{\chi}_+(\omega) \equiv \omega^2 \frac{1}{N} \sum_{k_+} \sum_n \tilde{\chi}_{k_+,n}(\omega), \quad (23)$$

and  $\tilde{\chi}'_{k_+,n}(\omega) \equiv d\tilde{\chi}_{k_+,n}(\omega)/d\omega$ . On the right side of Eq. (22), the first term  $\hat{\chi}_+(\omega)$  comes from simply ignoring the frequency detuning and the second term is a correction. We note that in our previous study,<sup>6</sup> a shift parameter was introduced to treat the effects from the frequency detuning. However, it is better to calculate the contributions from the second term directly because it turns out that, except for some simple cases, the previous method could introduce numerical errors. Similarly, one can approximate  $\tilde{\chi}_-(\omega)$  as

$$\begin{aligned}
\tilde{\chi}_-(\omega) &= \hat{\chi}_-(\omega) \\
&+ \omega^2 \frac{1}{N} \sum_{k_-} \sum_n \left[ -\bar{\omega} + \frac{1}{2}(\omega_{k_+} - \omega_n) \right] \tilde{\chi}'_{k_-,n}(\omega), \quad (24)
\end{aligned}$$

where

$$\hat{\chi}_-(\omega) \equiv \omega^2 \frac{1}{N} \sum_{k_-} \sum_n \tilde{\chi}_{k_-,n}(\omega). \quad (25)$$

Using the symmetries  $\tilde{\chi}_{k_-,n}(-\omega) = \tilde{\chi}_{k_+,n_+}(\omega)$  and  $\tilde{\chi}_{k_-,n_+}(-\omega) = \tilde{\chi}_{k_+,n_-}(\omega)$  (the latter is appropriate for the pure rotational bands only) mentioned above, one can show that

$$\hat{\chi}_-(-\omega) = \hat{\chi}_+(\omega), \quad (26)$$

and

$$\tilde{\chi}_-(-\omega) = \tilde{\chi}_+(\omega). \quad (27)$$

If one does not distinguish the two shapes  $\tilde{\chi}_+(\omega)$  and  $\tilde{\chi}_-(\omega)$  in the expression for  $\tilde{F}(\omega)$  given by Eq. (13) and replaces them by only one shape  $\tilde{\chi}(\omega)$ , one can pursue a similar derivation for  $\tilde{\chi}(\omega)$  and obtain



$$\tilde{\chi}(\omega) = \omega^2 \sum_k \sum_n \tilde{\chi}_{k;n} \left[ \omega - \frac{1}{2}(\omega_k + \omega_n) \right] \bigg/ \sum_k \rho_k |\boldsymbol{\mu}_k|^2. \quad (28)$$

A simple version  $\hat{\chi}(\omega)$ , defined by

$$\hat{\chi}(\omega) = \omega^2 \sum_k \sum_n \tilde{\chi}_{k;n}(\omega) \bigg/ \sum_k \rho_k |\boldsymbol{\mu}_k|^2, \quad (29)$$

can also be introduced. In this case, both  $\tilde{\chi}(\omega)$  and  $\hat{\chi}(\omega)$  become symmetric and, in addition, up to the first-order approximation,  $\tilde{\chi}(\omega)$  is the same as  $\hat{\chi}(\omega)$  because there is no net contribution to  $\tilde{\chi}(\omega)$  from the first derivative term of the Taylor series expansion of  $\tilde{\chi}_{k;n}[\omega - \frac{1}{2}(\omega_k + \omega_n)]$ .

In summary, we note that within this formalism no matter which functions are chosen for the line shape, in terms of them the symmetric spectral density  $\tilde{F}(\omega)$  always satisfies the detailed balance principle. The formalism outlined above was developed several years ago.<sup>6</sup> However, at that time, except for the simplest systems, such as CO<sub>2</sub>-Ar, to calculate converged line shapes for systems of interest in atmospheric applications was formidable. The main obstacle was the calculation involving a diagonalization procedure of the anisotropic potential that exhausts computer resources very quickly.

### C. The coordinate representation

Recently, we have developed a formalism based on the coordinate representation in which the eigenfunctions of the orientations of the system are chosen as the complete set in Hilbert space.<sup>1-3</sup> The advantage of introducing this representation is that the diagonalization of the potential becomes unnecessary and the main computational task is transformed to the carrying out of multidimensional integrations. For systems consisting of two linear molecules, or one linear and one asymmetric top molecule, or two asymmetric top molecules, the dimensionality is 7, 9, and 11, respectively. In addition, we have shown that using the Monte Carlo method, one is able to evaluate up to the nine-dimensional integrations required for systems such as H<sub>2</sub>O-N<sub>2</sub>.<sup>3</sup> Combined with techniques developed recently to handle sophisticated potential models,<sup>2</sup> one is able to implement realistic potentials for these systems and derive accurate, converged results for the far-wing line shapes and the corresponding absorption coefficients.

In the present study, we are interested in a system consisting of two H<sub>2</sub>O molecules. In order to reduce any unphysical effects, we base our study on formulas that satisfy the detailed balance principle exactly and have a higher accuracy in the short-time limit. Besides extending the Monte Carlo method to evaluate 11-dimensional integrations required for line shape calculations, we would like to answer some questions in depth. We want to know whether the line shapes are asymmetric and if they are, to find out the origin of the asymmetry. In other words, we want to know whether it is necessary to introduce two line shapes instead of one, and why they differ from each other. As expected, in comparison with our previous studies, this introduces extra difficulties. Fortunately, thanks to the coordinate representation

and the Monte Carlo method as two powerful tools to perform averages, and also to great advances in computers made in recent years, we are able to overcome these obstacles and make significant progress.

The details about the coordinate representation and the Monte Carlo method have been presented previously<sup>1-3</sup> and are not repeated here. We only report new features. Since we want to carry out band averages in a more sophisticated way, we have to introduce a positive and a negative resonance dipole operator in the Hilbert space of the absorber molecule denoted by  $\mu_m^>$  and  $\mu_m^<$ , respectively. The former is defined by

$$\mu_m^> = \sum_{E_j > E_i} \langle i | \mu_m | j \rangle | i \rangle \langle j |, \quad (30)$$

and the latter by

$$\mu_m^< = \sum_{E_j < E_i} \langle i | \mu_m | j \rangle | i \rangle \langle j |. \quad (31)$$

We note that for the vibrational bands  $j$  denotes a higher vibrational quantum number than  $i$  in Eq. (30) and vice versa in Eq. (31). Then, with Eqs. (8) and (23), one can rewrite  $\hat{\chi}_+(\omega)$  as a summation over  $\zeta$  and  $\eta$ ,

$$\hat{\chi}_+(\omega) = \omega^2 \frac{1}{N} \sum_{\zeta \eta} \tilde{H}_{\zeta \eta}(\omega) G_{(\zeta \eta)}^+, \quad (32)$$

where  $G_{(\zeta \eta)}^+$  are defined by

$$G_{(\zeta \eta)}^+ = \sum_m (\langle \zeta | \sqrt{\rho_b \rho_a}^{1/4} \mu_m^> \rho_a^{1/4} | \eta \rangle)^* \langle \zeta | \sqrt{\rho_b \rho_a}^{1/4} \mu_m^> \rho_a^{1/4} | \eta \rangle, \quad (33)$$

or

$$G_{(\zeta \eta)}^+ = \sum_m (\langle \zeta | \sqrt{\rho_b \rho_a}^{1/4} \mu_m^> \rho_a^{1/4} | \eta \rangle)^* \langle \zeta | \sqrt{\rho_b \rho_a}^{1/4} \mu_m^> \rho_a^{1/4} | \eta \rangle, \quad (34)$$

for the pure rotational bands and for the vibrational bands, respectively. For simplicity, we will only present formulas applicable for the pure rotational bands and simply mention differences between them and their vibrational analogs. In the expression for  $\hat{\chi}_+(\omega)$  given by Eq. (32), the summation terms are products of  $\tilde{H}_{\zeta \eta}(\omega)$  and  $G_{(\zeta \eta)}^+$ . The former are functions of  $\omega$  and their values depend on the interaction potential between the two molecules. The latter are common for all frequencies and their values are independent of the potential. With the coordinate representation, no matter how complicated the potential is, to calculate values of  $\tilde{H}_{\zeta \eta}(\omega)$  is straightforward since the potential is a diagonal operator. On the other hand, to obtain the  $G_{(\zeta \eta)}^+$  involves a lot of calculations, because they contain the density matrices that are differential operators. Fortunately, for a given temperature, these calculations need to be done only once since results obtained are applicable for all potential models. Thus, we can calculate them and store them in an input file.

In the coordinate representation, the basis functions  $|\zeta\rangle$  are nothing but the direct product  $|\delta(\boldsymbol{\Omega}_a - \boldsymbol{\Omega}_{a\zeta}) \otimes \delta(\boldsymbol{\Omega}_b - \boldsymbol{\Omega}_{b\zeta})\rangle$ , where the notations of  $|\delta(\boldsymbol{\Omega}_a - \boldsymbol{\Omega}_{a\zeta})\rangle$  and  $|\delta(\boldsymbol{\Omega}_b - \boldsymbol{\Omega}_{b\zeta})\rangle$  are used to represent specified orientations of the

absorber and the perturber molecules, respectively. Accordingly, one can separate the dependence of  $G_{(\zeta\eta)}^+$  on the absorber and on the perturber molecules and express it as the product of  $G_{a(\zeta\eta)}^+$  and  $G_{b(\zeta\eta)}$ ,

$$\begin{aligned} G_{(\zeta\eta)}^+ &= \sum_m (\langle \delta(\mathbf{Q}_a - \mathbf{Q}_{a\zeta}) | \rho_a^{1/4} \mu_m^> \rho_a^{1/4} | \delta(\mathbf{Q}_a - \mathbf{Q}_{a\eta}) \rangle)^* \\ &\quad \times \langle \delta(\mathbf{Q}_a - \mathbf{Q}_{a\zeta}) | \rho_a^{1/4} \mu_m \rho_a^{1/4} | \delta(\mathbf{Q}_a - \mathbf{Q}_{a\eta}) \rangle \\ &\quad \times |\langle \delta(\mathbf{Q}_b - \mathbf{Q}_{b\zeta}) | \sqrt{\rho_b} | \delta(\mathbf{Q}_b - \mathbf{Q}_{b\eta}) \rangle|^2 \\ &\equiv G_{a(\zeta\eta)}^+ G_{b(\zeta\eta)}. \end{aligned} \quad (35)$$

For the vibrational bands, the dipole moment operator  $\mu_m$  in Eq. (35) is replaced by  $\mu_m^>$ .

In comparison with  $G_{a(\zeta\eta)}^+$ , the expressions for  $G_{b(\zeta\eta)}$  are simpler because they do not contain the dipole operator. For the linear, symmetric top, and asymmetric top molecules, the explicit expressions for  $G_{b(\zeta\eta)}$  have been presented and the corresponding profiles have been discussed in our previous papers,<sup>1–3</sup> and we do not repeat them. With respect to  $G_{a(\zeta\eta)}^+$ , one has to derive the corresponding expressions valid for the linear, symmetric top, and asymmetric top molecules, respectively. We do not present all of them, rather only the last and the most complicated one applicable for

H<sub>2</sub>O. It is well known<sup>7,8</sup> that the wave functions of H<sub>2</sub>O,  $|j\tau m\rangle$ , can be expressed in terms of an expansion of symmetric-top wave functions  $|jkm\rangle$ ,

$$\begin{aligned} |j\tau m\rangle &= \sum_k U_{k\tau}^j |jkm\rangle \\ &= \sum_k U_{k\tau}^j \left[ (-1)^{m-k} \left( \frac{2j+1}{8\pi^2} \right)^{1/2} D_{-m,-k}^j(\alpha, \beta, \gamma) \right], \end{aligned} \quad (36)$$

where  $D_{m,k}^j(\alpha, \beta, \gamma) (= e^{-im\alpha} d_{m,k}^j(\beta) e^{-ik\gamma})$  is the rotational matrix. With Eq. (36), one is able to express  $G_{a(\zeta\eta)}^+$  as

$$G_{a(\zeta\eta)}^+ = \sum_L \sum_{KK'} A_{KK'}^{L+} D_{K,K'}^L(\alpha_{(\zeta\eta)}, \beta_{(\zeta\eta)}, \gamma_{(\zeta\eta)}), \quad (37)$$

where  $\alpha_{(\zeta\eta)}$ ,  $\beta_{(\zeta\eta)}$ , and  $\gamma_{(\zeta\eta)}$  are the three Euler angles used to represent a rotation resulting from two successive rotations, i.e.,

$$R(\alpha_{(\zeta\eta)}, \beta_{(\zeta\eta)}, \gamma_{(\zeta\eta)}) = R^{-1}(\alpha_\zeta, \beta_\zeta, \gamma_\zeta) R(\alpha_\eta, \beta_\eta, \gamma_\eta), \quad (38)$$

and the summation index  $L=0,1,2,\dots$ ; both indices  $K$  and  $K'$  run from  $-L$  to  $L$ . In the above expression, the coefficients  $A_{KK'}^{L+}$  are given by

$$\begin{aligned} A_{KK'}^{L+} &= \frac{1}{64\pi^4 N} (-1)^{1+L+K} \sum_{j_1\tau_1} \sum_{j_2\tau_2} (2j_1+1)(2j_2+1) \sqrt{g_{\tau_1} g_{\tau_2}} e^{-\beta[E(j_1,\tau_1)+E(j_2,\tau_2)]/4} \\ &\quad \times \sum_{\{j'_1\tau'_1\}+} \sum_{j'_2\tau'_2} (-1)^{j'_1+j'_2} \sqrt{(2j'_1+1)(2j'_2+1)} e^{-\beta[E(j'_1,\tau'_1)+E(j'_2,\tau'_2)]/4} W(j'_2 j'_1 j'_1, 1L) \\ &\quad \times \left( \sum_k (-1)^k U_{k\tau_1}^{j_1} U_{k-K\tau_2}^{j_2} C(j_1 j_2 L, kK-kK) \right) \left( \sum_{k'} (-1)^k U_{k'+K'\tau'_1}^{j'_1} U_{k'\tau'_2}^{j'_2} C(j'_1 j'_2 L, k'+K'-k'K') \right) \\ &\quad \times \left( \sum_{k_1} U_{k_1\tau_1}^{j_1} U_{k_1\tau'_1}^{j'_1} C(j_1 1 j'_1, k_1 0 k_1) \right) \left( \sum_{k_2} U_{k_2\tau_2}^{j_2} U_{k_2\tau'_2}^{j'_2} C(j_2 1 j'_2, k_2 0 k_2) \right), \end{aligned} \quad (39)$$

where  $E(j, \tau)$  are the energies of the state labeled by the quantum numbers  $j$  and  $\tau$ ,  $g_\tau$  is its nuclear spin degeneracy factor,  $C(j_1 j_2 L, kK-kK)$  is a Clebsch–Gordan coefficient,  $W(j'_2 j'_1 j'_1, 1L)$  is a Racah coefficient, and the summation over  $j'_1$  and  $\tau'_1$  indicated by a symbol  $\{j'_1\tau'_1\}+$  is limited to a range with  $E(j'_1\tau'_1) > E(j_1\tau_1)$ . In deriving the above expression, the body-fixed frame is chosen such that the dipole moment of H<sub>2</sub>O lies along its  $z$  axis (i.e., the  $II'$  representation). In addition, because the line shape functions are normalized with respect to the magnitude of the dipole moment, as shown by Eqs. (18), (20), and (21), the latter is assumed to be unity. We note that for the vibrational bands, the expression for  $A_{KK'}^{L+}$  is similar to that given above, except that the states labeled by  $j'_1\tau'_1$  and  $j'_2\tau'_2$  and the states labeled by  $j_1\tau_1$  and  $j_2\tau_2$  belong to a higher and a lower vibrational level, respectively. In addition, another limitation of  $E(j'_2\tau'_2) > E(j_2\tau_2)$  is also enforced in the summations.

With Eqs. (37) and (38), one can conclude that  $G_{a(\zeta\eta)}^+$  are three-dimensional distributions over three Euler angles used to represent a rotation of the molecule from the initial orientation to the final one, labeled by  $\zeta$  and  $\eta$ , respectively. With respect to  $\hat{\chi}_-(\omega)$ , one can introduce  $G_{a(\zeta\eta)}^-$  and write down similar equations to Eqs. (32) and (35). Meanwhile,  $G_{a(\zeta\eta)}^-$  can be given in terms of  $A_{KK'}^{L-}$  and  $D_{K,K'}^L(\alpha_{(\zeta\eta)}, \beta_{(\zeta\eta)}, \gamma_{(\zeta\eta)})$  in the same way as shown by Eq. (37). The expression for  $A_{KK'}^{L-}$  is almost identical to  $A_{KK'}^{L+}$ , shown by Eq. (39), except that the summation over  $j'_1$  and  $\tau'_1$  is limited to a range with  $E(j'_1\tau'_1) < E(j_1\tau_1)$ .

Although the calculations of  $A_{KK'}^{L+}$  and  $A_{KK'}^{L-}$  are straightforward, there are many summation loops involved. Usually one introduces a cut-off  $j_{\max}$  to exclude less populated states. It turns out that as  $j_{\max}$  increases, not only more CPU time is required to calculate each  $A_{KK'}^{L+}$  and  $A_{KK'}^{L-}$ , because the ranges

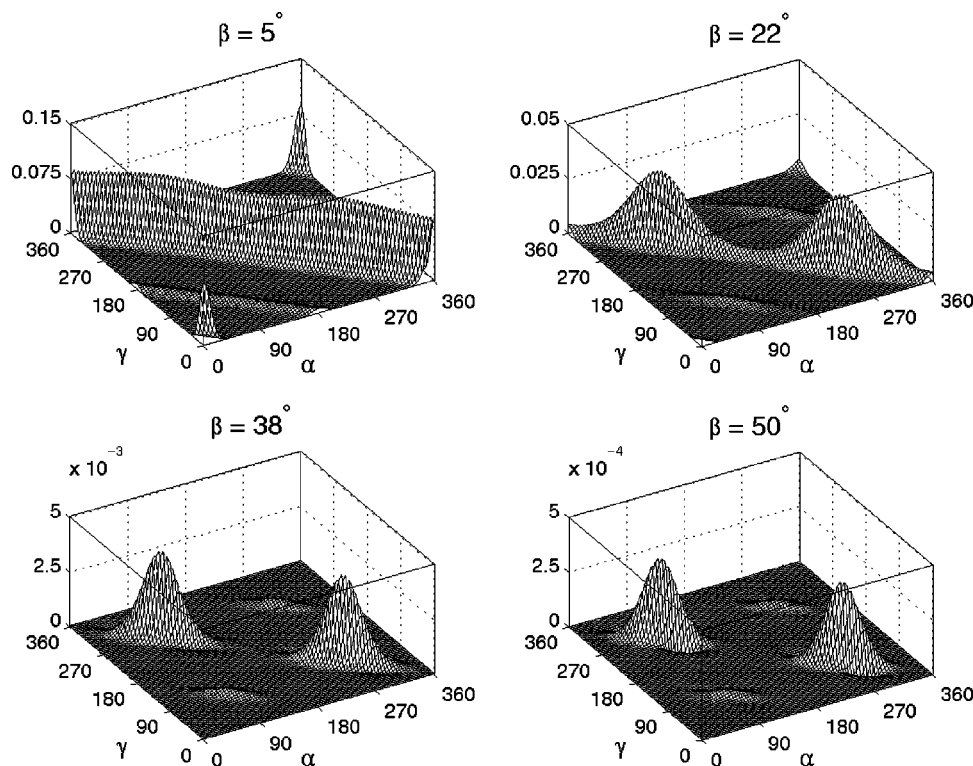


FIG. 1. The two-dimensional distribution of  $G_{a(\xi\eta)}^+(\alpha, \beta, \gamma)$  of  $\text{H}_2\text{O}$  over the Euler angles  $\alpha$  and  $\gamma$  obtained at  $T=296$  K for  $j_{\max}=26$ . The values of the Euler angle  $\beta$  is fixed and the four plots presented here correspond to  $\beta = 5^\circ, 22^\circ, 38^\circ$ , and  $50^\circ$ , respectively.

of loops become larger, but also the number to be evaluated increases quickly. Fortunately, one does not need to calculate all of them since some are identical and others are zero. For  $\text{H}_2\text{O}$ , due to the symmetry of  $U_{k\tau}^j$ , all the coefficients  $A_{KK'}^{L+}$  and  $A_{KK'}^{L-}$  are zero unless their indices  $K$  and  $K'$  have the same evenness or oddness. In addition, for the nonzero coefficients there are symmetries  $A_{KK'}^{L+} = A_{-K-K'}^{L+}$ ,  $A_{KK'}^{L-} = A_{-K-K'}^{L-}$ , and  $A_{KK'}^{L+} = A_{K'K}^{L-}$ . As a result, if one introduces a cut-off  $j_{\max}=23$  (which is the highest angular quantum number of the initial states listed in the pure rotational band of the HITRAN 92 database<sup>9</sup>), there are 18424 values of  $A_{KK'}^{L+}$  and 18424 of  $A_{KK'}^{L-}$  needed to be evaluated. If one uses an even higher cut-off  $j_{\max}=26$ , these numbers become 26235. By utilizing a dozen CPUs, we are able to manage the latter in less than two days. We note that to obtain these coefficients is the most costly calculational part in the present study.

After all  $A_{KK'}^{L+}$  and  $A_{KK'}^{L-}$  are available, we can easily calculate  $G_{a(\xi\eta)}^+$  and  $G_{a(\xi\eta)}^-$ , which are three-dimensional distributions over the Euler angles  $\alpha_{(\xi\eta)}$ ,  $\beta_{(\xi\eta)}$ , and  $\gamma_{(\xi\eta)}$ . In cases where no confusion results, the subscripts of these Euler angles are omitted. However, it is better to express them as distributions over their two sensitive variables  $\beta$  and  $u$  [ $\equiv(\alpha+\gamma)/2$ ] and one insensitive one  $v$  [ $\equiv(\alpha-\gamma)/2$ ]. The explicit expression for  $G_{a(\xi\eta)}^+$  used in the numerical calculations, is given by

$$G_{a(\xi\eta)}^+(\beta, u, v) = \sum_L \sum_{KK'} A_{KK'}^{L+} \epsilon_{KK'} d_{KK'}^L(\beta) \times \{ \cos[(K+K')u] \cos[(K-K')v] - \sin[(K+K')u] \sin[(K-K')v] \}, \quad (40)$$

where the ranges of the indices  $L$ ,  $K$ , and  $K'$  are from 0 to  $2j_{\max}$ , from 0 to  $L$ , and from  $-L$  to  $L$ , respectively;  $\epsilon_{KK'} = 1$  for  $K=0$ , and  $\epsilon_{KK'}=2$  otherwise. The expression for  $G_{a(\xi\eta)}^-$  is similar to Eq. (40), except a replacement of  $A_{KK'}^{L+}$  by  $A_{KK'}^{L-}$ . However, due to the symmetry  $A_{KK'}^{L+} = A_{K'K}^{L-}$  mentioned above,  $G_{a(\xi\eta)}^+(\beta, u, v)$  does not differ from  $G_{a(\xi\eta)}^-(\beta, u, v)$  significantly. In fact, it is easy to show that

$$G_{a(\xi\eta)}^+(\beta, u, v) = G_{a(\xi\eta)}^-(\beta, u, -v). \quad (41)$$

This means that with respect to the sensitive variables  $\beta$  and  $u$ , they have same distribution patterns. Meanwhile, with respect to the insensitive  $v$ , one is the others' mirror image.

Because  $G_{a(\xi\eta)}^+(\beta, u, v)$  and  $G_{a(\xi\eta)}^-(\beta, u, v)$  are three dimensional, it is impossible to plot their profile in one figure. We calculate several two-dimensional distributions of  $G_{a(\xi\eta)}^+(\alpha, \beta_0, \gamma)$  over the Euler angles  $\alpha$  and  $\gamma$  at 296 K obtained with the fixed  $\beta_0 = 5^\circ, 22^\circ, 38^\circ$ , and  $50^\circ$ , respectively, and present their corresponding three-dimensional plots in Fig. 1. From the figure, one can easily see that the magnitudes of  $G_{a(\xi\eta)}^+$  decreases very fast as  $\beta_0$  increases. More specifically, for  $\beta_0 = 22^\circ, 38^\circ$ , and  $50^\circ$  the magnitudes decrease by about one order each. In addition, these  $G_{a(\xi\eta)}^+$  exhibit symmetry with respect to the axes  $(\alpha+\gamma)/2$  and  $(\alpha-\gamma)/2$ . In order to show the profile of  $G_{a(\xi\eta)}^+$  at 296 K over the two sensitive variables  $\beta$  and  $u$ , we calculate its average over  $v$  and present the resulting two-dimensional distributions in Fig. 2. One has to imagine that the profile shown in Fig. 2 extends along another dimension, i.e., the  $v$  axis that is perpendicular to the  $\beta-u$  plane and is missing in the figure. Furthermore, the range of extension along the  $v$  axis varies from the minimum 0 at  $u=0$  and  $2\pi$  to the maximum  $2\pi$  at  $u=\pi$ . As shown in Fig. 2, there are five sharp peaks located along the  $u$  axis at  $u=0, \pi/2, \pi, 3\pi/2$ , and  $2\pi$ , respectively,

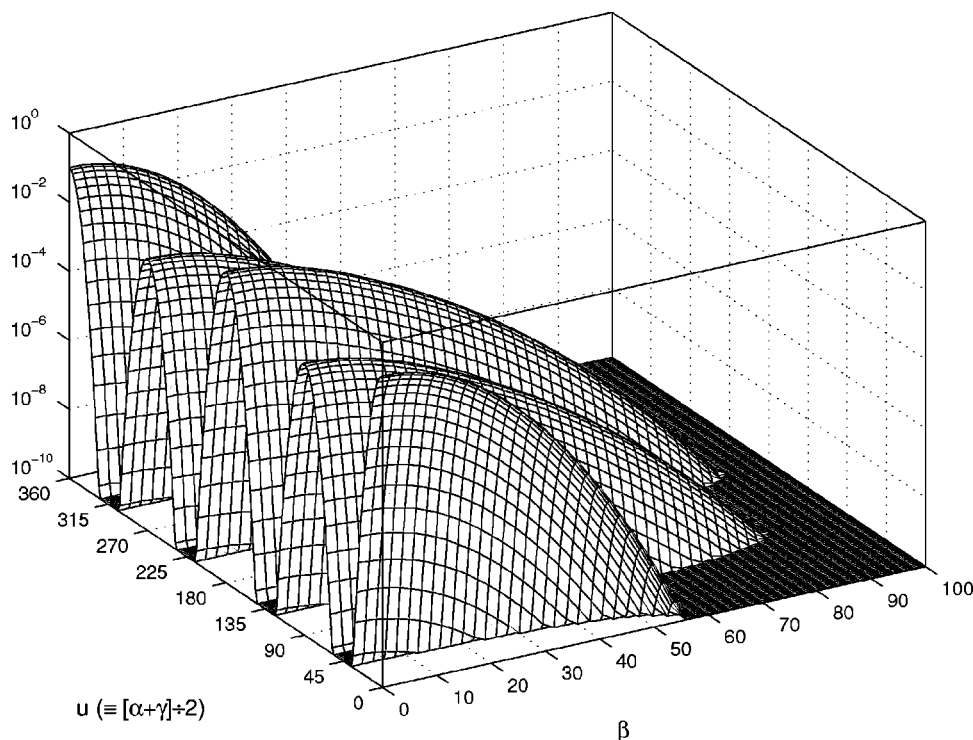


FIG. 2. The two-dimensional distribution of  $G_{a(\xi\eta)}^+(\beta, u, v)$  of H<sub>2</sub>O over the two sensitive variables  $\beta$  and  $u$  obtained at  $T=296$  K for  $j_{\max}=26$ . This distribution results from the averaging  $G_{a(\xi\eta)}^+(\beta, u, v)$  over the one insensitive variable  $v$ . In contrast with Fig. 1, a logarithmic coordinate is used for the  $G_{a(\xi\eta)}^+(\beta, u, v)$  axis.

and they are symmetric with respect to the plane  $u = \pi$ . The magnitudes of these peaks decrease very fast as  $\beta$  increases. We note that in contrast with Fig. 1, a logarithmic coordinate is used to plot the magnitudes. From Figs. 1 and 2, one can conclude that the peak at  $u = \pi$  is dominant. We do not present the profiles of  $G_{a(\xi\eta)}^+$  for other temperatures, but simply mention that they have similar patterns, but the peaks become lower and wider as the temperature decreases. On the other hand, it is unnecessary to present similar figures for  $G_{a(\xi\eta)}^-$  because one can easily obtain them from Figs. 1 and 2. In fact, Figs. 1 and 2 are also applicable for  $G_{a(\xi\eta)}^-$  except that one has to switch the labels  $\alpha$  and  $\gamma$  in Fig. 1. Finally, we note that because  $G_{a(\xi\eta)}^+(\beta, u, v)$  and  $G_{a(\xi\eta)}^-(\beta, u, v)$  are independent of the potential, it is wise to calculate them first and store them in files. Then, when one carries out repeated calculations for  $\hat{\chi}_+(\omega)$  and  $\hat{\chi}_-(\omega)$  to optimize the potential models, one does not need to evaluate the values of  $G_{a(\xi\eta)}^+(\beta, u, v)$  and  $G_{a(\xi\eta)}^-(\beta, u, v)$  again. In addition, using the interpolation method one can easily obtain their values for a random selection of  $\beta$ ,  $u$ , and  $v$  from these input files. Otherwise, one has to independently evaluate them about  $10^7$  times in the Monte Carlo calculations.

#### D. Contributions from frequency detuning

So far, our discussion has been focused on how to apply the coordinate representation for calculating  $\hat{\chi}_+(\omega)$  and  $\hat{\chi}_-(\omega)$ . In order to calculate  $\tilde{\chi}_+(\omega)$  and  $\tilde{\chi}_-(\omega)$ , one has to go further by adding contributions from the frequency detuning. We briefly explain a method used to obtain the second term of Eq. (22) associated with  $\tilde{\chi}_+(\omega)$ . In comparison with evaluating the first term  $\hat{\chi}_+(\omega)$ , the only additional obstacle is that the integrand contains a derivative  $\tilde{\chi}'_{k_+;n}(\omega)$ . In practice, except for special cases in which analytic expressions

for this derivative are available, to evaluate values of  $\tilde{\chi}'_{k_+;n}(\omega)$  is much more difficult than  $\tilde{\chi}_{k_+;n}(\omega)$  because a numerical subroutine is required to obtain the former from the latter. Given the fact that there are about  $10^7$  random selections in the Monte Carlo calculations, this means that this subroutine must be called  $10^7$  times. Fortunately, except for this part, the other parts of the second term do not depend on the frequency. Therefore, it is better to reverse the order of the derivative and the summation (i.e., integral) operations. In other words, instead of  $(1/N)\sum_{k_+}\sum_n[\bar{\omega} - \frac{1}{2}(\omega_{k_+} + \omega_n)]\tilde{\chi}'_{k_+;n}(\omega)$ , we can calculate a new term given by  $(1/N)\sum_{k_+}\sum_n[\bar{\omega} - \frac{1}{2}(\omega_{k_+} + \omega_n)]\tilde{\chi}_{k_+;n}(\omega)$ . The results obtained are a function of the frequency represented by a set of values of the integrations and a set of corresponding frequencies. Then, with the numerical subroutine, one is able to obtain the derivatives that are just the second term we want to calculate. With this technique, the subroutine is called only once and the cost to calculate the second term of Eq. (22) is comparable to the first.

The same method used for  $\hat{\chi}_+(\omega)$  explained in Sec. II C is also applicable for evaluating this new term. We do not repeat a detailed discussion, but simply mention things that are different. In this case, a new set of coefficients  $B_{KK'}^{L+}$  can be introduced whose expression is almost the same as  $A_{KK'}^{L+}$  given by Eq. (39), except a factor of  $\{\bar{\omega} - \frac{1}{2}[E(j'_1\tau'_1) - E(j_1\tau_1) + E(j'_2\tau'_2) - E(j_2\tau_2)]\}$  is inserted into the inside of summation loops over the indices  $j_1$ ,  $\tau_1$ ,  $j_2$ ,  $\tau_2$ ,  $j'_1$ ,  $\tau'_1$ ,  $j'_2$ , and  $\tau'_2$ . Similarly, one can introduce a set of coefficients  $B_{KK'}^{L-}$  associated with the second term of Eq. (24) for  $\tilde{\chi}_-(\omega)$  whose expression is the same as  $B_{KK'}^{L+}$  except the summation over  $j'_1$  and  $\tau'_1$  is limited to a range with  $E(j'_1\tau'_1) < E(j_1\tau_1)$ . We note that in comparison with  $A_{KK'}^{L+}$  and  $A_{KK'}^{L-}$ ,



$B_{KK'}^{L+}$  and  $B_{KK'}^{L-}$  have similar symmetries  $B_{KK'}^{L+} = B_{-K-K'}^{L+}$  and  $B_{KK'}^{L-} = B_{-K-K'}^{L-}$ , except  $B_{KK'}^{L+} = -B_{K'K}^{L-}$ . Then, one can introduce two three-dimensional distributions associated with  $B_{KK'}^{L+}$  and  $B_{KK'}^{L-}$ , respectively, and store their values in two input files the same way as  $G_{a(\zeta\eta)}^+(\beta, u, v)$  and  $G_{a(\zeta\eta)}^-(\beta, u, v)$ . Finally, by comparing these two distributions, their patterns are closely related to each other, as shown by Eq. (41), except one has to add a minus sign on the right side since their values become opposite.

As expected, to evaluate  $B_{KK'}^{L+}$  and  $B_{KK'}^{L-}$  requires considerable CPU time, and the costs are approximately the same as for  $A_{KK'}^{L+}$  and  $A_{KK'}^{L-}$ . In practice, for specified  $L$ ,  $K$  and  $K'$ , one does not need to calculate the four coefficients separately, rather one can evaluate all of them simultaneously.

### E. A Monte Carlo calculation of 11-dimensional integrations

As an example, we explain how to calculate  $\hat{\chi}_+(\omega)$  from Eq. (23) in detail. In the coordinate representation, the summation of  $\tilde{H}_{\zeta\eta}(\omega)G_{(\zeta\eta)}^+$  over  $\zeta$  and  $\eta$  becomes a 11-dimensional integration of  $\tilde{H}_{\zeta\eta}(\omega)G_{(\zeta\eta)}^+$  over the Euler angles  $\beta_{a\zeta}$ ,  $\gamma_{a\zeta}$ ,  $\alpha_{b\zeta}$ ,  $\beta_{b\zeta}$ ,  $\gamma_{b\zeta}$ ,  $\alpha_{a\eta}$ ,  $\beta_{a\eta}$ ,  $\gamma_{a\eta}$ ,  $\alpha_{b\eta}$ ,  $\beta_{b\eta}$ , and  $\gamma_{b\eta}$  in which the first five (including  $\alpha_{a\zeta}=0$ ) specify the initial orientations of the system and the last six specify the final ones. We note that due to the rotational symmetry of the whole system, one can always assume  $\alpha_{a\zeta}=0$ . For such high dimensionality, the Monte Carlo method is the only way to evaluate the integrals.

It is well known that in the Monte Carlo computation, it is important to distinguish the sensitive and insensitive variables of the integrand, and to incorporate this into the integration variables since this enables one to tailor the important sampling and to reduce the variance dramatically. In the present case, the integrand is a product of  $\tilde{H}_{\zeta\eta}(\omega)$  and  $G_{(\zeta\eta)}^+$ . With respect to their variables, the former is a smooth function, as shown by Eq. (9), but the latter's values vary wildly and could differ from each other by many orders of magnitude. This means that the sensitivity of integrand is mainly determined by  $G_{(\zeta\eta)}^+$ , or more specifically, by  $G_{a(\zeta\eta)}^+$  and  $G_{b(\zeta\eta)}$ . We note that  $G_{a(\zeta\eta)}^+$  and  $G_{b(\zeta\eta)}$  depend on relative orientations between the initial and final positions of the absorber and perturber molecules, respectively. Therefore, it is proper to represent the final orientations of the system labeled by  $\eta$  in terms of the body-fixed frames instead of the space-fixed frame. The body-fixed frames introduced here are those attached to the two molecules at their initial orientational positions. For the asymmetric-top molecule, one chooses  $\alpha_\zeta$ ,  $\beta_\zeta$ ,  $\gamma_\zeta$ ,  $\alpha_{(\zeta\eta)}$ ,  $\beta_{(\zeta\eta)}$ , and  $\gamma_{(\zeta\eta)}$  instead of  $\alpha_\zeta$ ,  $\beta_\zeta$ ,  $\gamma_\zeta$ ,  $\alpha_\eta$ ,  $\beta_\eta$ , and  $\gamma_\eta$  as variables. However, similar to the behavior of  $G_{b(\zeta\eta)}$  explained in our previous study,<sup>3</sup> the sensitivity of  $G_{a(\zeta\eta)}^+$  on its two variables  $\alpha_{(\zeta\eta)}$  and  $\gamma_{(\zeta\eta)}$  is interwoven such that neither is a sensitive or insensitive variable, but their combinations  $u_{(\zeta\eta)}$  and  $v_{(\zeta\eta)}$  are. Therefore, in order to well characterize the sensitivity, a replacement of  $\alpha_{(\zeta\eta)}$ ,  $\beta_{(\zeta\eta)}$ , and  $\gamma_{(\zeta\eta)}$  by  $\beta_{(\zeta\eta)}$ ,  $u_{(\zeta\eta)}$ , and  $v_{(\zeta\eta)}$  as vari-

ables in  $G_{a(\zeta\eta)}^+$  is appropriate. The same conclusion is also true for  $G_{b(\zeta\eta)}$ . This is a further step necessary to evaluate 11-dimensional integrations because, in comparison with 7 or 9-dimensional ones, not only the dimensionality becomes higher, but also the distributions of the integrand become more nonuniform. However, in order to incorporate these new choices for the integration variables, one has to pay extra attention to their ranges. More specifically, since  $u_{(\zeta\eta)}$  varies from 0 to  $2\pi$  and  $v_{(\zeta\eta)}$  varies from  $-u_{(\zeta\eta)}$  to  $u_{(\zeta\eta)}$  when  $0 \leq u \leq \pi$ , and from  $u_{(\zeta\eta)} - 2\pi$  to  $2\pi - u_{(\zeta\eta)}$  when  $\pi \leq u \leq 2\pi$ , the integration volume becomes a lozenge-shaped area. Because the algorithm VEGAS<sup>10</sup> is designed for carrying out integrations over rectangular volumes, one cannot incorporate the integration variables directly. Therefore, we have modified VEGAS such that the new version enables one to evaluate integrations over a volume containing a lozenge-shape area. Then, with respect to the sensitivity, the dependence of the integrand on all integration variables is well characterized. This enables one to fully exploit the power of the Monte Carlo method. As a result, numerical tests show that with a few more random selections than before, one is able to evaluate the 11-dimensional integrations successfully.

The above discussion is also applicable for evaluating other 11-dimensional integrations, i.e., those for  $\hat{\chi}_-(\omega)$ , and for the frequency detuning correction terms of  $\tilde{\chi}_+(\omega)$  and  $\tilde{\chi}_-(\omega)$  because their integrands have similar features. Numerical tests show that with the modified version of VEGAS, we are also able to evaluate these as well.

### F. Potential models

Based on the progress mentioned so far, we are able to calculate converged line shapes for  $\text{H}_2\text{O}-\text{H}_2\text{O}$  without or with the frequency detuning correction, i.e.,  $\hat{\chi}_+(\omega)$  and  $\hat{\chi}_-(\omega)$ , or  $\tilde{\chi}_+(\omega)$  and  $\tilde{\chi}_-(\omega)$ , from potential models provided unless they are too complicated (e.g., those consisting of several decades of terms and parameters). There are several potential models available in literatures, such as the HF,<sup>11</sup> CI,<sup>12</sup> Watts,<sup>13</sup> RWK1,<sup>14</sup> and RWK2 model.<sup>14</sup> We have tested some of them to calculate the line shapes and the corresponding absorption coefficients. Unfortunately, it turns out that the results obtained from these models predict too much absorptions in comparison with experimental data. It has been shown in our previous study<sup>2,3</sup> that the far-wing shape is very sensitive to the angular gradients of the potential. The reason is that contributions to the line shape come mainly from energy contour areas at which large angular gradients of the potential are exhibited while the potential values themselves are relatively small or even negative. We expect that such features would not fully manifest their effects on other physical measurements on which these models were developed. Therefore, the failure of these models is not surprising.

As an alternative, we assume that the potential for  $\text{H}_2\text{O}-\text{H}_2\text{O}$  consists of a Coulomb interaction represented by a site-site model, a short range repulsive interaction represented by another site-site model, and an isotropic attractive dispersion interaction proportional to  $-1/r^6$ . For each  $\text{H}_2\text{O}$ , there are two positive point charges  $+q$  located at the H at-

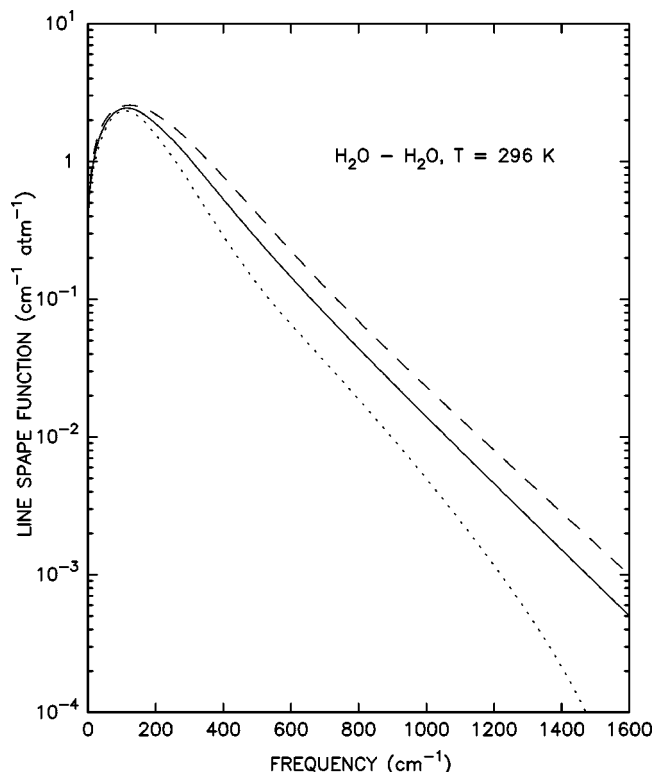


FIG. 3. The self-broadened far-wing line shape of H<sub>2</sub>O (in units of cm<sup>-1</sup> atm<sup>-1</sup>) as a function of frequency  $\omega$  (in units of cm<sup>-1</sup>) for  $T = 296$  K. The dashed curve represents  $\tilde{\chi}_+(\omega)$  calculated from the positive resonance line average and the dotted curve represents  $\tilde{\chi}_-(\omega)$  calculated from the negative resonance line average. The solid curve is  $\tilde{\chi}(\omega)$  which is the mean of  $\tilde{\chi}_+(\omega)$  and  $\tilde{\chi}_-(\omega)$ .

oms and one negative point charge  $-2q$  at a position along its symmetry axis a distance  $d$  from the O atom. (A positive value of  $d$  means the charge  $-2q$  is located on the same side as the center of mass.) In addition, we assume that there are three repulsive force centers: two located at the two H atoms and one at the O atom, and the repulsive interactions have a form  $A_{ij}e^{-r_{ij}/\rho_{ij}}$ , where  $r_{ij}$  are distances between force centers, and  $A_{ij}$  and  $\rho_{ij}$  are adjustable parameters. Accordingly, the potential  $V(r, \mathbf{\Omega}_a, \mathbf{\Omega}_b)$  considered here is given by

$$V(r, \mathbf{\Omega}_a, \mathbf{\Omega}_b) = \sum_{i \in a} \sum_{j \in b} \frac{q_i q_j}{r_{ij}} + \sum_{i \in a} \sum_{j \in b} A_{ij} e^{-r_{ij}/\rho_{ij}} - \frac{B}{r^6}, \quad (42)$$

and it contains seven adjustable parameters:  $A_{OO}$ ,  $\rho_{OO}$ ,  $A_{OH}$ ,  $\rho_{OH}$ ,  $A_{HH}$ ,  $\rho_{HH}$ , and  $B$ . The values of  $q = 0.60$  (a.u.) and  $d = 0.4991$  (a.u.) are determined such that they match the well-known dipole moment value 1.8546 D and yield quadrupole moments  $\theta_{cc} = -2.319$  D Å,  $\theta_{aa} = 2.635$  D Å, and  $\theta_{bb} = -0.316$  D Å, which are reasonable in comparison with experimental values  $\theta_{cc} = -2.50$  D Å,  $\theta_{aa} = 2.63$  D Å, and  $\theta_{bb} = -0.13$  D Å.<sup>15</sup> We adopt the potential form given by (42) and search for a set of potential parameters that enables us to obtain satisfactory results for several properties of a dilute H<sub>2</sub>O gas; e.g., the absorption coefficient, the second virial coefficient, and the differential cross section.

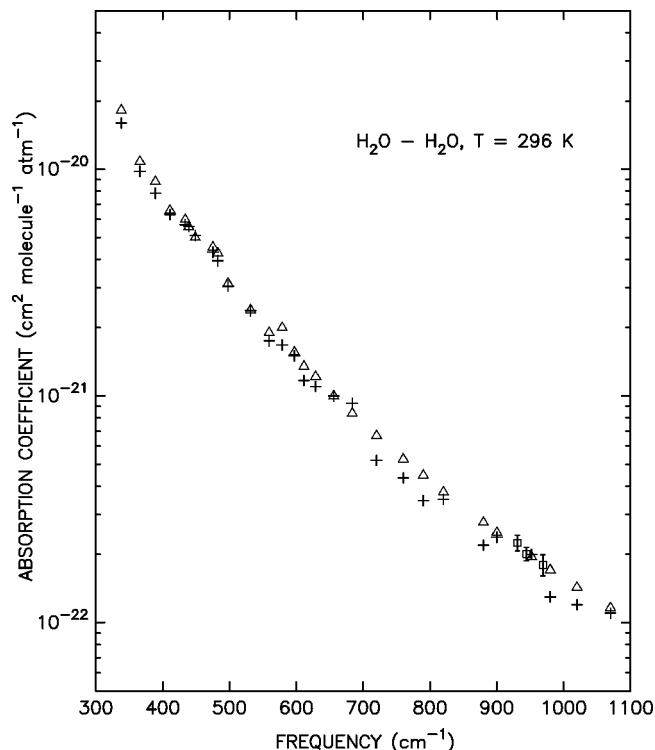


FIG. 4. The calculated self-broadened absorption coefficient (in units of cm<sup>2</sup> molecule<sup>-1</sup> atm<sup>-1</sup>) at  $T = 296$  K in the 300–1100 cm<sup>-1</sup> spectral region is represented by  $\Delta$ . For a comparison, the experimental values of Burch *et al.* are denoted by  $+$  and those from Cormier *et al.* are denoted by  $\square$ , along with their error bars.

### G. General features and numerical results for the line shapes

We have presented the line shape formulas applicable for both the pure rotational band and vibrational bands. But, in the present study, the numerical calculations are carried out for the former because, not only is this the strongest band of H<sub>2</sub>O, but also most of the continuum absorption measurements are performed in its high-frequency wing.

It is worthwhile to report general features of line shapes found from numerous test calculations before we present more specific results. First of all, we find that differences between  $\hat{\chi}_+(\omega)$  and  $\hat{\chi}_-(\omega)$  calculated from the same potential are always less than numerical errors. The formulas used to get  $\hat{\chi}_+(\omega)$  and  $\hat{\chi}_-(\omega)$  are the same, but the input files representing the two distributions  $G_{a(\zeta\eta)}^+(\beta, u, v)$  and  $G_{a(\zeta\eta)}^-(\beta, u, v)$ , respectively, are different. However, these two distributions differ from each other only slightly. In fact, as explained above, they exhibit the same profiles over two sensitive variables  $\beta$  and  $u$ , and are mirror images over the insensitive  $v$ . In cases where the potential contains cyclic coordinates, it is easy to show analytically that these two distributions must yield the same line shapes. For more general cases, given the fact that  $G_{a(\zeta\eta)}^+(\beta, u, v)$  and  $G_{a(\zeta\eta)}^-(\beta, u, v)$  differ from each other as discussed above, we suspect that effects resulting from these differences could cancel out in the averaging processes when the integrations are evaluated by about  $10^7$  random selections. In the present study, we do not seek a general and rigorous proof of this finding, rather we assume it. Then, we can draw the impor-

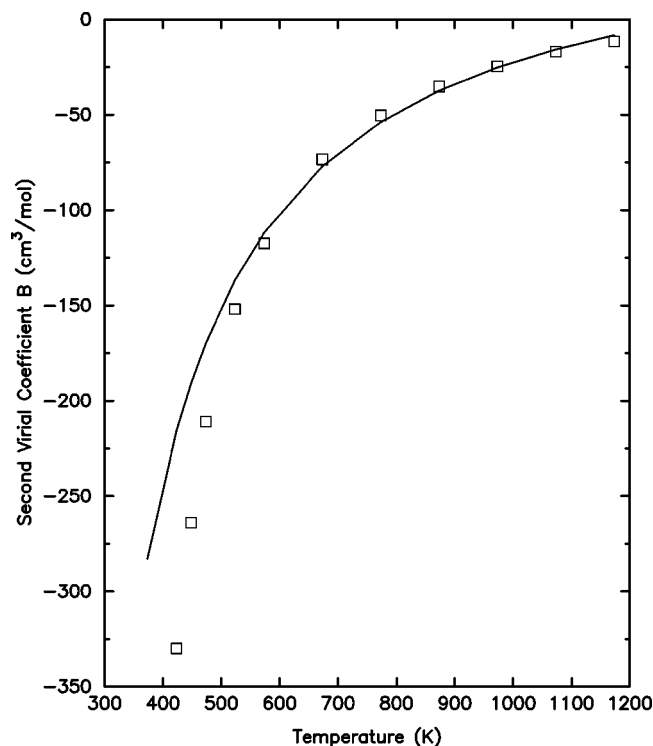


FIG. 5. The calculated second virial coefficients (in units of  $\text{cm}^3 \text{mol}^{-1}$ ) as a function of temperature is represented by a solid line. The experimental data are denoted by  $\square$ .

tant conclusion that by not considering the frequency detuning correction, the line shape obtained from the formalism satisfying the detailed balance is symmetric. In other words, if one does not consider the frequency detuning correction, one only needs to introduce one line shape function.

Second, we find that the calculated contributions from the frequency detuning associated with  $\tilde{\chi}_+(\omega)$  are opposite to those associated with  $\tilde{\chi}_-(\omega)$ , and the differences between their magnitudes are always less than numerical errors. This indicates that these correction contributions have the same magnitudes, but with different signs; this is not surprising since we have already noted our finding for  $\hat{\chi}_+(\omega)$  and  $\hat{\chi}_-(\omega)$ . In general, the values of the correction contribution for  $\tilde{\chi}_+(\omega)$  are positive and those for  $\tilde{\chi}_-(\omega)$  are negative for  $\omega > 0$  and *vice versa* for  $\omega < 0$ . In addition, we find that the correction contributions are significant, especially at high frequencies, but they tend to become negligible near the line center.

Now, we are ready to present some results. We find that by adopting  $A_{\text{OO}}/k = 1.05 \times 10^7 \text{ K}$ ,  $\rho_{\text{OO}} = 0.245 \text{ \AA}$ ,  $A_{\text{OH}}/k = 2.0 \times 10^3 \text{ K}$ ,  $\rho_{\text{OH}} = 0.36 \text{ \AA}$ ,  $A_{\text{HH}}/k = 4.0 \times 10^2 \text{ K}$ ,  $\rho_{\text{HH}} = 0.46 \text{ \AA}$ , and  $B/k = 9.0 \times 10^3 \text{ K}$ , one is able to obtain  $\tilde{\chi}_+(\omega)$  and  $\tilde{\chi}_-(\omega)$  such that the calculated absorption at 296 K can fit the experimental results in the spectral region 300–1100  $\text{cm}^{-1}$  very well. We note that because this window region is located on the high-frequency side of the pure rotational band, the calculated absorption arises mainly from the contributions of  $\tilde{\chi}_+(\omega)$ . The two line shapes  $\tilde{\chi}_+(\omega)$  and  $\tilde{\chi}_-(\omega)$  at 296 K, together with their mean  $\hat{\chi}(\omega)$ , are plotted in Fig. 3. As shown in the figure, the magnitudes of  $\tilde{\chi}_+(\omega)$  are larger than  $\tilde{\chi}_-(\omega)$  and the relative gaps between them

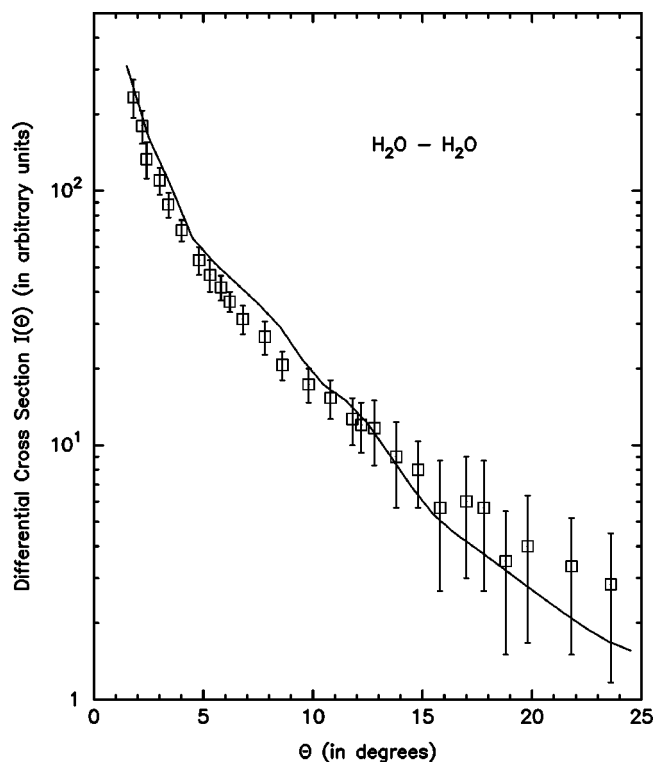


FIG. 6. The calculated differential cross section (in arbitrary units) as a function of the laboratory scattering angle  $\theta$  is represented by a solid line. The experimental values of Duquette are denoted by  $\square$ .

increase significantly as  $\omega$  increases. The corresponding self-broadened absorption coefficients in the spectral region 300–1100  $\text{cm}^{-1}$  based on HITRAN 92 data are plotted in Fig. 4, together with the experimental results of Burch *et al.*<sup>16</sup> and some recent measurements of Cormier *et al.*<sup>17</sup> Using this potential, we calculated the second virial coefficients at several temperatures<sup>18</sup> and compare them with experimental data<sup>14</sup> in Fig. 5. In addition, the calculated differential cross section together with experimental data<sup>19</sup> are plotted in Fig. 6. We note that all these physical quantities are associated with dilute water vapor, and as shown by these figures, the agreements between the theoretical predictions and the laboratory measurements are good.

Based on the same potential model, we calculated the two line shapes  $\tilde{\chi}_+(\omega)$  and  $\tilde{\chi}_-(\omega)$  for several temperatures ranging from 220 to 330 K that are of interest in the atmospheric applications and the corresponding absorption coefficients. Some of  $\tilde{\chi}_+(\omega)$  obtained for 220, 240, 260, 280, 300, and 320 K with frequencies ranging from –1600 to 1600  $\text{cm}^{-1}$  are presented in Fig. 7, and the corresponding  $\tilde{\chi}_-(\omega)$  are their reflections about the  $\omega = 0$  axis. As shown in the figure, these  $\tilde{\chi}_+(\omega)$  and  $\tilde{\chi}_-(\omega)$  are asymmetric and their magnitudes increase as the temperature decreases. We note that the line shapes  $\tilde{\chi}_+(\omega)$  and  $\tilde{\chi}_-(\omega)$  presented here do not include a factor  $1/\omega^2$ , as shown in Eq. (13). If one wants to compare them to other line shapes (e.g., a Lorentzian), one has to multiply them by the factor  $1/\omega^2$ . Also, the magnitude of  $\tilde{\chi}_+(\omega)$  or  $\tilde{\chi}_-(\omega)$  as  $\omega \rightarrow 0$  should approach the Lorentzian half-width, although the present theory is not valid in this limit. It is clear, however, that the theoretical shapes are

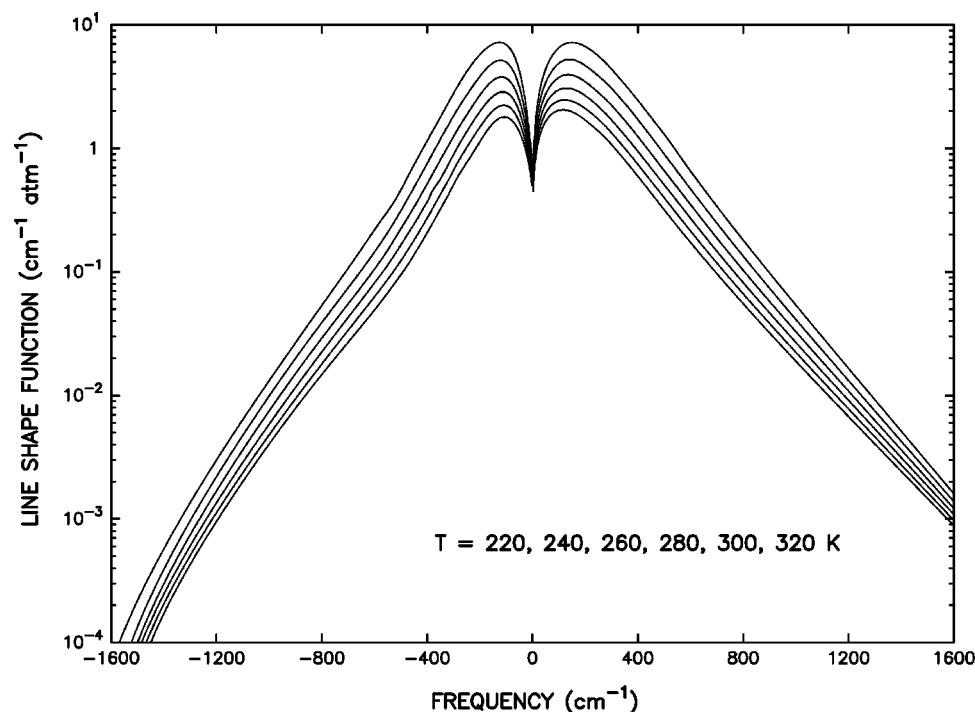


FIG. 7. The self-broadened far-wing line shapes  $\tilde{\chi}_+(\omega)$  of H<sub>2</sub>O (in units of  $\text{cm}^{-1} \text{atm}^{-1}$ ) as a function of frequency  $\omega$  (in units of  $\text{cm}^{-1}$ ) obtained for  $T=220, 240, 260, 280, 300$ , and  $320$  K; these are represented by six curves in order from top to bottom. The frequency  $\omega$  varies from  $-1600$  to  $1600$   $\text{cm}^{-1}$ . The corresponding  $\tilde{\chi}_-(\omega)$  are reflections of  $\tilde{\chi}_+(\omega)$  about the  $\omega=0$  axis.

super-Lorentzian for the displacements up to around  $400$   $\text{cm}^{-1}$  and then become sub-Lorentzian for larger displacements. In fact, the line shape must approach zero at least as fast as an exponential. This can be shown from the analyticity of the correlation function; the successive derivatives of  $C(t)$  in the  $t=0$  limit correspond to moments of the line shape in frequency space. Because the derivatives are all finite, this implies that all the moments of the line shape are also finite and, therefore, the line shape must approach zero faster than any inverse power of  $\omega$ . In Fig. 8, we present all

the calculated absorption coefficients in the window region  $600$ – $1250$   $\text{cm}^{-1}$ . We note that for a specified frequency  $\omega$ , we exclude completely any contribution from lines that are within  $[\omega - 25 \text{ cm}^{-1}, \omega + 25 \text{ cm}^{-1}]$  in the calculations. As shown by Fig. 8, the strong, negative temperature dependence of self-continuum is clearly demonstrated.

### III. DISCUSSIONS AND CONCLUSIONS

In comparison with our previous studies on the far-wing line shape, there are several important advances that have

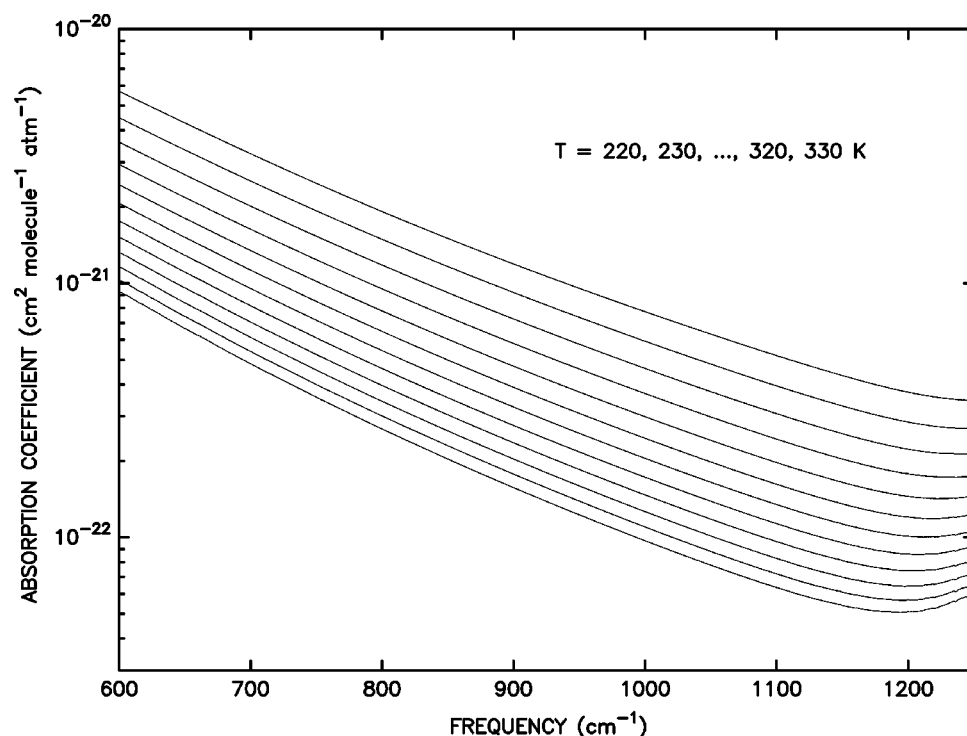


FIG. 8. The self-broadened absorption coefficient (in units of  $\text{cm}^2 \text{molecule}^{-1} \text{atm}^{-1}$ ) in the window region  $600$ – $1250$   $\text{cm}^{-1}$  calculated for  $T=220, 230, 240, 250, 260, 270, 280, 290, 300, 310, 320$ , and  $330$  K in order from top to bottom. A cut-off  $25 \text{ cm}^{-1}$  is used to exclude completely any contribution of lines that are closer than this limit.



been made in the present study. First of all, by clearly distinguishing the sensitive and insensitive variables and by modifying the Monte Carlo subroutine used previously to handle integrations whose volume is not rectangular, the effectiveness of the important sampling is enhanced significantly. As a result, by accounting for random selections of the order of  $10^7$  (which is comparable to or slightly more than that required for lower-dimensionality cases), one is able to evaluate 11-dimensional integrations.

Second, we have carried out numerical calculations based on the formalism that satisfies the detailed balance principle exactly and has a higher accuracy in the short-time limit. As expected, this increases the difficulty because the evaluation of the integrands requires more calculations. As shown by Eqs. (3) and (4), within this formalism the dipole moment operator appears in formulas in such a way that it is always sandwiched by the density matrix. However, these two operators have different characters: one depends on the coordinates only while the other contains differential operators. No matter what kind of representation is chosen, the sandwiched operators require more loops to evaluate their values. As in our previous studies, we use the coordinate representation because it enables us to include more populated states; we also introduce the distribution functions and store them in files because it enables us to obtain values of the integrand with less CPU time. But, to calculate these distributions with a high cut-off  $j_{\max}$  requires long CPU times. We note that for temperatures of interest in atmospheric applications,  $j_{\max}=23$  is enough, but for higher temperatures, a higher  $j_{\max}$  would be necessary. With these input files, to obtain values of the integrand becomes relatively easy. Combining the technique mentioned above to reduce the number of random selection to the order of  $10^7$ , one is able to complete the evaluation of 11-dimensional integrations and to obtain a line shape in one day with one workstation.

Finally, by carrying out band averages in a more sophisticated way, we can calculate the two line shape functions. In addition, the effects resulting from the frequency detuning have been taken into account in the averaging processes. We note that except for the simplest system, e.g.  $\text{CO}_2\text{--Ar}$ ,<sup>6</sup> the latter has not been done previously. In fact, most calculations are similar to those without including the frequency detuning correction, except the integrand contains a derivative. As explained above, we have developed a technique that enables one to overcome this obstacle and calculate the frequency detuning corrections.

Based on numerous test calculations of line shapes during the course of study, we can draw several important conclusions. It is necessary to consider the frequency detuning correction because the effect on the line shape is significant, especially in the high-frequency region. However, this effect shows up only when one distinguishes the positive and the negative resonance lines and carries out the band average over them separately. In other words, we have demonstrated that the line shapes obtained from the two band averages are asymmetric and we have found that this asymmetry results from the frequency detuning effect, or, more specifically, from the distribution of lines within the band of interest. In addition, we find that for the pure rotational band the mag-

nitudes of  $\bar{\chi}_+(\omega)$  are significantly larger than  $\bar{\chi}_-(\omega)$  for  $\omega > 0$  and *vice versa* for  $\omega < 0$ , and these gaps become larger as  $\omega$  increases. We note that the conclusion concerning the asymmetry claimed here is applicable for the band average line shapes and has nothing to do with individual lines.

Finally, we would like to make a few comments on the vibrational bands. We expect the main conclusions about the line shapes for the pure rotational band would remain true, but some different features could show up because the contributions to  $\bar{\chi}_+(\omega)$  and  $\bar{\chi}_-(\omega)$  from the frequency detuning terms depend strongly on the band structure. We expect that the more unevenly and the more widely the lines are distributed within the band of interest, the contributions from the frequency detuning corrections will increase and the more  $\bar{\chi}_+(\omega)$  differs from  $\bar{\chi}_-(\omega)$ . It is well known that the line distributions of the vibrational bands are quite different from that for the pure rotational one. The former's lines are, more or less, evenly located on both sides of the band centers, but the latter's are always on the high-frequency side because the band center is zero. We note that according to the definition, the average positive resonance frequency  $\bar{\omega}$  introduced here is not the band center. These two are very close for the vibrational bands, but are quite different for the pure rotational band. We expect that for the vibrational band the frequency detuning corrections could become smaller. This means that  $\bar{\chi}_+(\omega)$  and  $\bar{\chi}_-(\omega)$  differ from each other by smaller amounts. Meanwhile, we could not draw any conclusion about which magnitude is larger because this is related to the special structure of the pure rotational band. It has been known for years that the line shapes for  $\text{CO}_2$  derived from experimental data are asymmetric and they are not the same for different bands.<sup>20,21</sup> So far, there has been no theoretical explanation as to why the different bands have different shapes without assuming that the interaction depends sensitively on the vibrational quantum numbers, which seems unlikely to be true. We think that both from the theoretical and practical points of view, to investigate the lines shapes for different bands is an interesting subject to pursue.

## ACKNOWLEDGMENTS

This work was supported in part by the Department of Energy Interagency Agreement under the Atmospheric Radiation Measurement Program, by NASA through Grants No. NAG5-6314, No. NAG5-8269, and No. NAGW-4693. The authors would like to thank the National Energy Research Supercomputer (Livermore, CA) for computer time and facilities provided. Also, J. G. Cormier is acknowledged for providing his results prior to publication.

<sup>1</sup>Q. Ma and R. H. Tipping, J. Chem. Phys. **108**, 3386 (1998); Q. Ma, R. H. Tipping, C. Boulet, and J.-P. Bouanich, Appl. Opt. **38**, 599 (1999).

<sup>2</sup>Q. Ma and R. H. Tipping, J. Chem. Phys. **111**, 5909 (1999).

<sup>3</sup>Q. Ma and R. H. Tipping, J. Chem. Phys. **112**, 574 (2000).

<sup>4</sup>Q. Ma, R. H. Tipping, and C. Boulet, J. Quant. Spectrosc. Radiat. Transf. **59**, 245 (1998).

<sup>5</sup>R. W. Davies, R. H. Tipping, and S. A. Clough, Phys. Rev. A **26**, 3378 (1982).

<sup>6</sup>Q. Ma, R. H. Tipping, and C. Boulet, J. Chem. Phys. **104**, 9678 (1996).

<sup>7</sup>R. L. Cook and F. C. De Lucia, Am. J. Phys. **39**, 1433 (1971).

<sup>8</sup>G. W. King, R. M. Hainer, and P. C. Cross, J. Chem. Phys. **11**, 27 (1943).

- <sup>9</sup>L. S. Rothman, R. R. Gamache, R. H. Tipping *et al.*, J. Quant. Spectrosc. Radiat. Transf. **48**, 469 (1992).
- <sup>10</sup>*Numerical Recipes in Fortran 77*, edited by W. H. Press, S. A. Teukolsky, W. T. Vetterling, and B. P. Flannery (Cambridge University Press, Cambridge, 1992).
- <sup>11</sup>H. Popkie, H. Kistenmacher, and E. Clementi, J. Chem. Phys. **59**, 1325 (1973); H. Kistenmacher, G. C. Lie, H. Popkie, and E. Clementi, *ibid.* **61**, 546 (1974).
- <sup>12</sup>O. Matsuoka, E. Clementi, and M. Yoshimine, J. Chem. Phys. **64**, 1351 (1976); G. C. Lie, E. Clementi, and M. Yoshimine, *ibid.* **64**, 2314 (1976).
- <sup>13</sup>R. O. Watts, Chem. Phys. **26**, 367 (1977).
- <sup>14</sup>J. R. Reimers, R. O. Watts, and M. L. Klein, Chem. Phys. **64**, 95 (1982).
- <sup>15</sup>J. Verhoeven and A. Dymanus, J. Chem. Phys. **52**, 3222 (1970).
- <sup>16</sup>D. E. Burch, Proc. SPIE **277**, 28 (1981); D. E. Burch and D. A. Gryvnak, Report No. AFGL-TR-79-0054, 1979; D. E. Burch and R. L. Alt, Report No. AFGL-TR-84-0128, 1984.
- <sup>17</sup>J. G. Cormier, R. Ciurylo, and J. R. Drummond, J. Chem. Phys. **116**, 1030 (2002).
- <sup>18</sup>A. J. Stone, A. Dullweber, M. P. Hodges, P. L. A. Popelier, and D. J. Wales, "Orient: A Program for studying interactions between molecules," Version 3.2, University of Cambridge, 1995.
- <sup>19</sup>G. Duquette, Ph.D. thesis, University of Waterloo, Waterloo, Canada, 1977.
- <sup>20</sup>D. E. Burch, D. A. Gryvnak, R. R. Patty, and C. E. Bartky, J. Opt. Soc. Am. **59**, 267 (1969).
- <sup>21</sup>M. V. Tonkov, N. N. Filippov, V. V. Bertsev, J. P. Bouanich, N. Van-Thanh, C. Brodbeck, J. M. Hartmann, C. Boulet, F. Thibault, and R. Le Doucen, Appl. Opt. **35**, 4863 (1996).